GDCh

**Research Article**

*Angewandte*
*Chemie*
*International Edition*
www.angewandte.org

**Batteries**

# Constructing Matching Interfaces by Amorphous Engineering for Enhanced Lithium Ion Transport in Quasi-Solid-State Lithium–Iodine Batteries

*Jiapei Gu[+], Chenxu Dong[+], Yuxin Zhu, Haoyun Liu, Juan Ji, Yongkun Yu, Changning Ma, Cheng Zhou,\* Liqiang Mai, and Xu Xu\**

**Abstract:** Quasi-solid-state lithium–iodine (Li–$I_2$) batteries have shown prospects as their high theoretical capacity, high safety, and abundant iodine resources. However, the interface between the crystalline filler and the flexible polymer skeleton of composite solid electrolytes exhibits inadequate bonding, leading to higher interface energy and sluggish migration dynamics of Li⁺. In this work, a continuous interface solid electrolyte is designed by combining the atomic structure rearrangement of metal-organic framework (MOF) to achieve interface coupling between MOF and aramid fiber. Based on the experimental results and theoretical calculations, the amorphous engineering promotes Li⁺ migration and polyiodide confinement effects for Li–$I_2$ batteries. The batteries show a high capacity of 170.7 mAh g⁻¹ at 5 C and achieve a capacity retention rate of 97.8% after 450 cycles. More impressively, the batteries achieve a long life of 3000 cycles at the high current density of 20 C with a good capacity retention of 94.1%. This work reveals the mechanism of coupled interface with structure matching in Li⁺ migration and polyiodide integration process, providing guidance for the design of novel composite solid electrolytes to achieve high-performance Li–$I_2$ batteries.

## Introduction

Rechargeable lithium–iodine (Li–$I_2$) batteries have been recognized as a promising candidate to meet the huge demand for high-energy-density energy storage systems.[1] Li–$I_2$ batteries use Li metal as the anode and iodine as the cathode, with a high discharge voltage plateau (3.65 V vs. Li/Li⁺) and high theoretical capacity (211 mAh g⁻¹).[2] Additionally, the iodine cathode has a lower cost thanks to the abundant iodine resources in the Earth's oceans. In particular, the superior electrochemical reaction kinetics of the iodine cathode make it have good rate performance.[3,4] Every coin has two sides, and it is precisely the high solubility of iodine species in organic electrolytes that causes detrimental shuttle effects, resulting in rapid deterioration of capacity and battery failure.[5,6] Simultaneously, the concentration of iodine species dissolved in the electrolyte increases, which results in a decline

in ionic conductivity.[7] In addition, the safety risks and a decline in the cycling life would result from the uncontrollable dendrite formation of the Li metal anodes during cycling.

Recent studies have demonstrated that the quasi-solid-state electrolytes (QSSEs) are a promising approach to address the aforementioned core challenges of both the $I_2$ cathode and the Li anode simultaneously,[8] thereby enhancing the safety and electrochemical performance of Li–$I_2$ batteries.[9,10] Regarding QSSEs, among the diverse categories of solid electrolytes developed, composite polymer solid electrolytes (CPEs) effectively integrate the advantageous properties of polymeric solid electrolytes, such as enhanced flexibility and superior interfacial contact, with the high ionic conductivity and broad electrochemical stability characteristic of inorganic solid electrolytes.[11–13] This integration addresses the limitations associated with slow ion dynamics and suboptimal Li⁺ selective transport in polymeric systems. Recent studies have reported the incorporation of metal-organic frameworks (MOFs) as fillers in novel polymer-based electrolytes,[14] leveraging their porous ion channels and tunable chemical environments to significantly enhance both ionic conductivity and single-ion transport capability in composite quasi-solid electrolytes.[15–17] For instance, Chen et al. introduced a robust and flexible QSSE characterized by a "tree-trunk" architecture. The cellulose-based framework is covered in an in situ grown MOF layer to generate hierarchical ion channels that facilitate rapid Li⁺ migration dynamics and exceptional durability.[18] Pang et al. developed a fluorine-modified MOF to assemble high-performance QSSEs. The chemical interactions at the F-sites within MOF-stabilized PVDF-HFP chains, combined

[*] J. Gu[+], C. Dong[+], Y. Zhu, H. Liu, J. Ji, Y. Yu, C. Ma, Dr. C. Zhou, Prof. L. Mai, Prof. X. Xu
State Key Laboratory of Advanced Technology for Materials Synthesis and Processing, School of Materials Science and Engineering, Wuhan University of Technology, Wuhan 430070, China
E-mail: zhoucheng1208@whut.edu.cn
xuxu@whut.edu.cn

J. Gu[+], Prof. X. Xu
Zhongyu Feima New Material Technology Innovation Center (Zhengzhou) Co., Ltd., High Technology Industrial Development Zone, Zhengzhou 450001, P.R. China

[+] Both authors contributed equally to this work.

⌨ Additional supporting information can be found online in the Supporting Information section

with disordered vibrations, improve charge transfer and Li$^+$ transport properties.[19]

Despite its great promise, the rigid lattice structure of crystalline MOF is usually poorly combined with the flexible polymer framework.[20] Due to the nonadaptation of the crystal lattice, the crystalline-amorphous interface is formed.[21,22] The local high electric field caused by the high interfacial energy between crystalline MOF and polymer seriously hinders the migration of Li$^+$ in CPEs.[23,24] Eliminating the interface mismatch between crystalline MOF and polymer is anticipated to significantly enhance Li$^+$ transport dynamics.[25] Additionally, amorphous MOFs are expected to form an interfacial coupling with polymers owing to their distinctive structural characteristics of short-range order and long-range disorder.[26,27] Therefore, there is an urgent need to explore novel combinations of amorphous MOFs and polymers, combining hydrogen bond interactions and dipole moment interactions, on the one hand optimizing interfacial contact between MOF fillers and polymers, and promoting the migration of Li$^+$ in CPEs.[28,29] On the other hand, by changing the electron configuration through atomic structure rearrangement, the interaction with polyiodide is enhanced, and the shuttle effect is effectively inhibited in Li–I$_2$ batteries. Unfortunately, so far, there are no reports of amorphous–amorphous integrated CPEs between polymers and MOF fillers that can achieve continuous and fast ion transport and effectively inhibit shuttle effects.

In this work, the atomic structure rearrangement of amorphous Fe-MOF is controlled to match with the aramid fiber skeleton, achieving the interface coupling. The continuous amorphous MOFs exhibit enhanced interfacial bonding strength without the limitations imposed by crystalline-amorphous interface structure mismatch when combined with amorphous polymers while retaining the advantages of crystalline MOFs. In addition, the dense packing structure of amorphous MOFs shortens the transport distance of Li$^+$, completely eliminates the transport gap caused by interspaces, and facilitates the charge transfer. Amorphous MOFs have more twisted metal nodes, which alters the electronic configuration and thus enhances the interaction with the polyiodides and mitigates the shuttling problem. As a demonstration, the batteries with continuous interface QSSEs exhibit satisfactory capacity and cycle stability. Impressively, quasi-solid-state Li–I$_2$ batteries employing the novel electrolyte delivered a long-term cycle life exceeding 3000 cycles at 20 C with a remarkable capacity retention rate of 94.1%. This unique amorphous–amorphous architecture obtained encouraging results for developing novel high-performance composite QSSEs for Li–I$_2$ batteries, and it provides valuable insights into the advancement of QSSEs in related fields.

## Results and Discussion

Considering the importance of interfacial compatibility between the MOF filler and the polymer scaffold, the introduction of the amorphous MOF (namely R-MOF) reduces interfacial energy and accelerates the migration of Li$^+$ in

continuous interface QSSEs. Equally significant is the fact that R-MOF possesses a higher binding energy with polyiodides by altering the electron configuration and exposing more twisted metal nodes through its electron mismatch, which effectively inhibits the shuttle effect in lithium–iodine (Li–I$_2$) batteries (Figure 1a). To simultaneously enhance the safety characteristics and electrochemical performance of QSSEs, the high-temperature resistant aramid nanofiber (ANF) was chosen as the scaffold for the in situ growth of MOF. By manipulating the synthesis temperature, R-MOF with a disordered structure was successfully synthesized under low temperature (room temperature), while crystalline MOF (namely T-MOF) with an ordered structure was obtained at high temperatures (100 °C). The fabrication of novel continuous interface QSSE membranes via a typical in situ growth method is schematically shown in Figure S1.

The structural and morphological characterizations of MOF and ANF-MOF were conducted using scanning electron microscopy (SEM) and cryo-scanning transmission electron microscopy (Cryo-STEM). T-MOF exhibits a regular 2D quadrilateral nanosheet morphology with a large size (Figure S2), while R-MOF displays an irregular morphology with a much smaller size than T-MOF (Figure S3), which may be attributed to its amorphous structure. Meanwhile, the energy-dispersive X-ray spectroscopy (EDS) elemental mappings of T-MOF and R-MOF indicate the uniform distribution of Fe, N, O, and P elements inside the MOFs (Figures S4 and S5). As shown in Figure S6, the pristine ANF exhibits a typical smooth nanofiber morphology and amorphous structure. After the amorphous R-MOF is grown in situ, the interface of the two achieves interfacial coupling, forming a uniformly integrated amorphous configuration (Figure 1d). In contrast, crystalline T-MOF demonstrates distinct lattice fringes and well-defined diffraction patterns (see inset of Figure 1b), which cannot be well combined with ANF to form a uniform configuration. As shown in Figures 1c,e, S7, and S8, the EDS elemental mappings of T-ANF-MOF and R-ANF-MOF indicate the homogeneous distribution of R-MOF on the surfaces of ANF nanofibers, while T-MOF does not. The same morphological characteristics are shown in the SEM images (Figures S9 and S10). Furthermore, the cross-section morphologies show that the thicknesses of ANF, T-ANF-MOF, and R-ANF-MOF membranes are 13, 17, and 26 μm, respectively (Figure S11).

The X-ray diffraction (XRD) patterns were further conducted to validate the crystallization structure of synthesized samples. The obtained T-MOF shows three distinct diffraction peaks around 6.6°, 12.9°, and 19.2°, the R-MOF only shows one low-intensity diffraction peak around 6.0°, suggesting its structure is disordered.[30] The amorphous property of R-MOF was further demonstrated (Figure S12). In addition, it can be clearly observed that the typical ANF and MOF diffraction peaks in the T-ANF-MOF and R-ANF-MOF membranes further confirm the successful growth of MOFs on the surface of ANF nanofibers (Figure 1f). Furthermore, Fourier transform infrared (FT-IR) spectra were conducted to characterize the particular structural information of different examples. As shown in Figures 1g and S13, the characteristic peaks at ~1646, ~1541, ~1506, ~1308, and ~1015 cm$^{-1}$, which are attributed
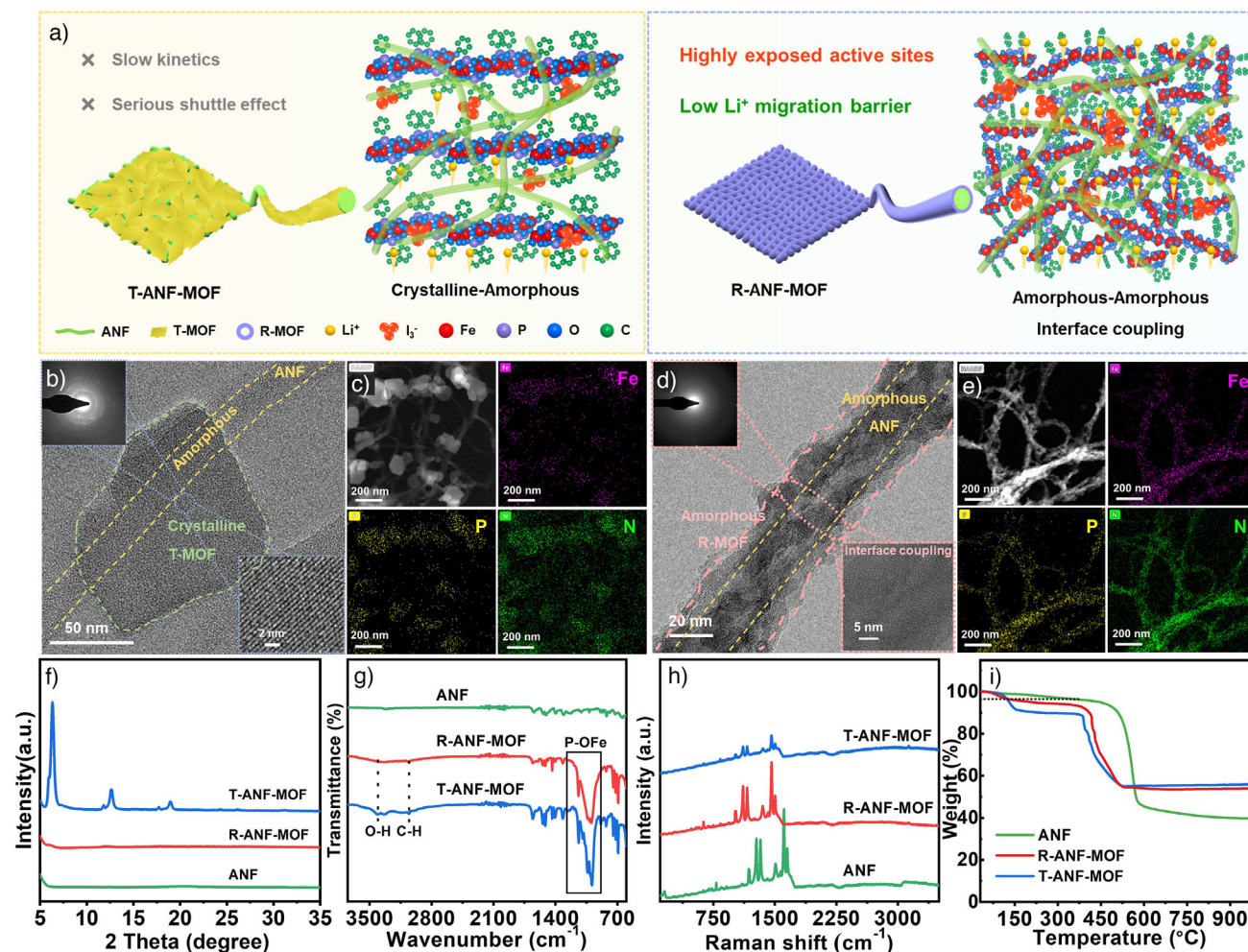
**Figure 1.** a) The schematic of the working mechanism of R-ANF-MOF and T-ANF-MOF in Li–I₂ batteries. b)–e) Cryo-STEM images and elemental mapping images of T-ANF-MOF (b, c) and R-ANF-MOF (d, e) (the insets show the SAED pattern). f) XRD patterns, g) FTIR spectra, h) Raman spectra, and i) TGA curves of ANF, R-ANF-MOF, and T-ANF-MOF membranes.

to the C=O stretching in amide, N–H deformation and C–N stretching vibration, C=C stretching vibration of the aromatic ring, Ph–N stretching vibration, and in-plane C–H bending vibration in phenyl, respectively. Additionally, the appearance of the P–OFe bonds at the region between 1200–900 cm$^{-1}$ corresponds to the coordination of Fe with the O atom in the phosphonate group, demonstrating the introduction of the MOF structure.[31] In comparison to the distinct peaks observed for T-MOF, the vibrational peaks of R-MOF cannot be obviously distinguished, which may be due to its amorphous properties. In Raman spectroscopy (Figures 1h and S14), the characteristic peaks of the benzene ring from ANF and the characteristic peaks of the Fe–O and P–O bonds from MOF are all preserved intact in R-ANF-MOF and T-ANF-MOF.[31,32] Note that the peaks of the Fe–O–P bond in R-MOF are not obvious enough, which aligns with the previously confirmed amorphization. Besides, the contents of Fe, C, P, O, and H elements in the R-MOF and T-MOF are further determined according to the inductively coupled plasma optical emission spectrometry (ICP-OES) and elemental analysis (EA). As shown in Tables S1 and S2,

the content of each element in R-MOF is similar to that in T-MOF, demonstrating that their elemental composition is extremely similar. The specific surface areas and pore structures of the MOFs are tested by N₂ adsorption/desorption method. Both R-MOF and T-MOF show a typical type III isotherm, with R-MOF possessing a marginally higher specific surface area of 35.98 m² g$^{-1}$ compared to 32.83 m² g$^{-1}$ for T-MOF. In addition, R-MOF exhibits a smaller pore size distribution (Table S3). The increased specific surface area and reduced pore size distribution are attributed to the size decrease resulting from the amorphization of R-MOF (Figure S15). Additionally, thermogravimetric analysis (TGA) curves demonstrate the degradation temperature of the pure ANFs and MOFs up to 500 °C. Therefore, ANF-MOFs exhibit favorable thermal stability owing to the architectural support of ANFs (Figures 1i and S16). Moreover, the thermal stability of various membranes from 20 to 200 °C was further confirmed as shown in Figure S17. In contrast to the severe dimension shrinkage of PP separator only at 150 °C, the R-ANF-MOF and T-ANF-MOF membranes showed no dimensional shrinkage even at 200 °C because of the intrinsic
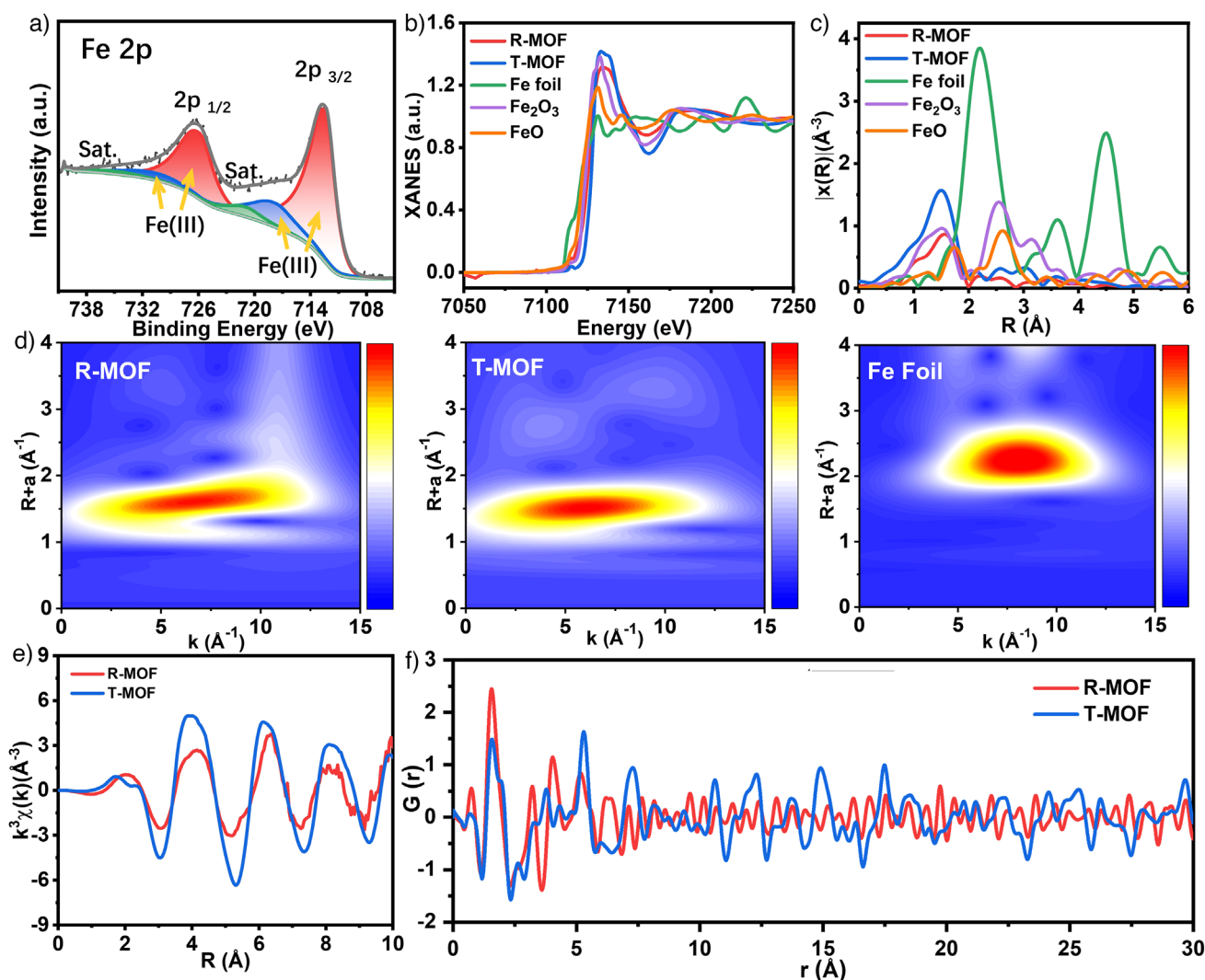
**Figure 2.** a) High-resolution XPS spectra of Fe 2p for the R-MOF. b) Fe K-edge XANES spectra and c) $k^3$-weighted FT-EXAFS spectra in the R space of R-MOF, T-MOF, Fe foil, $Fe_2O_3$, and FeO. d) WT-EXAFS data of R-MOF, T-MOF, and Fe foil. e) The $k^3$-weighted FT-EXAFS spectra in the k space and f) PDF analysis for R-MOF and T-MOF.

thermal resistance of ANF and the uniform distribution of MOF, ensuring the safe operation of Li–I$_2$ batteries.

The X-ray photoelectron spectroscopy (XPS) profile analysis was conducted to demonstrate the existence and chemical environment of Fe, O, C, and P elements in the R-MOF and T-MOF (Figures 2a and S18–S20). The high-resolution O 1s spectrum displays the presence of peaks at 533.2 eV in both R-MOF and T-MOF, which can be attributed to hydroxyl or water. Besides, the Fe–O peak is observed at 531.6 and 531.5 eV for R-MOF and T-MOF, respectively, which represents the P–OH and P=O after the coordination with Fe. The high-resolution spectra of P 2p display the binding energy of the P 2p$_{3/2}$ and P 2p$_{1/2}$ orbitals for R-MOF (133.7 and 132.9 eV, respectively) and T-MOF (133.6 and 132.9 eV, respectively), which represent the P=O and P–O bonds, respectively. Figure 2a exhibits the high-resolution spectra of Fe 2p, and the binding energy of the Fe 2p$_{3/2}$ and Fe 2p$_{1/2}$ orbitals for R-MOF (726.1 and 712.7 eV, respectively) are higher than that for T-MOF (725.5

and 712.2 eV, respectively), which can be attributed to a lower electron density of Fe center in R-MOF. The slight disparities in the binding energies of R-MOF and T-MOF may be attributed to structural and electronic distribution changes caused by amorphization.[33] Additionally, the local structure and coordination environment of R-MOF and T-MOF were investigated using synchrotron-radiation-based X-ray absorption near-edge structure (XANES) spectra and Fourier-transformed extended X-ray absorption fine structure (FT-EXAFS) characterization. The Fe K-edge XANES spectroscopy, analyzed alongside Fe foil, $Fe_2O_3$, FeO, R-MOF, and T-MOF (Figure 2b), shows the transitions of R-MOF and T-MOF closely resemble those of $Fe_2O_3$, indicating that the oxidation states of Fe in both samples are approximately +3. To further investigate the coordination information, the FT-EXAFS spectra exhibit the dominant peaks in R-MOF and T-MOF at 1.56 and 1.51 Å, respectively, which is attributed to the Fe–O path in R-space (Figure 2c). The decreased intensity observed for R-MOF suggests an enhanced disorder

in the Fe center.[34] The samples have no characteristic peaks corresponding to Fe-Fe paths at 2.20 Å (Fe foil) or 2.62 Å (Fe$_2$O$_3$). Further wavelet transform (WT) investigation was performed to clarify the clear information of backscattered atoms in R and k space. The contour plots of both R-MOF and T-MOF display a WT maxima at about 5.9 Å (Figures 2d and S21). Moreover, as shown in Figure 2e, the presence of similar oscillation curves of EXAFS spectra in the k space indicates a comparable structural configuration of the Fe center, the increased distortion in the metal node accounts for the shift in location of the R-MOF wave peak. To further delve deeper into the atom-to-atom distances, we have conducted the X-ray pair distribution function (PDF) analysis of R-MOF and T-MOF to determine the degree of order in atomic arrangement (Figure 2f). The PDF curves exhibit identical peaks in the lower *r* range, manifesting that the short-range structural characteristics of R-MOF exhibit a resemblance to those observed in T-MOF. In addition, the PDF curves exhibit the distinct peaks in the higher *r* range, comparison with T-MOF reveals a less obvious vibrational peaks for R-MOF in the higher *r* range, thus demonstrating the absence of a well-defined order over long distances.

The electrochemical stability and ion transport ability of the obtained QSSEs were investigated via electrochemical stability window, exchange current density, Li$^+$ conductivity ($\sigma$), Li$^+$ transference number ($t_{Li^+}$), and Li stripping/plating kinetics. As shown in Figure S22, linear sweep voltammetry (LSV) profiles were employed to identify the electrochemical stability window of the ANF, R-ANF-MOF, and T-ANF-MOF membranes. The exceptional durability and chemical inertness of ANF positively conduce to the R-ANF-MOF and T-ANF-MOF QSSE membranes, contributing to a favorable electrochemical stable window (all above 4.7 V) that determines the superior electrochemical stability of R-ANF-MOF. To estimate the charge-transfer kinetics at the electrolyte–electrode interface, the exchange current density was determined through the fitting of the Tafel curve, which was acquired from the cyclic voltammetry (CV) curves of the Li||Li symmetric cells with the scan rate of 10 mV s$^{-1}$ (Figure S23). As shown in Figure 3a, the exchange current density value of R-ANF-MOF (0.63 mA cm$^{-2}$) was significantly higher than that of ANF (0.19 mA cm$^{-2}$) and T-ANF-MOF (0.35 mA cm$^{-2}$), suggesting that the electrochemical reaction dynamics of R-ANF-MOF are enhanced. Furthermore, the temperature-dependent electrochemical impedance spectroscopy (EIS) of QSSE membranes was implemented by a model of stainless steel|QSSE|stainless steel symmetric cells at the temperature range from 20 to 80 °C. As shown in Figure S24, the R-ANF-MOF (3.7 Ω) exhibits the minimum bulk resistance compared with the ANF (31.3 Ω) and T-ANF-MOF (5.7 Ω) at 20 °C. The Li$^+$ conductivity ($\sigma$) calculated from the EIS curves further verifies the ion transport capability, the R-ANF-MOF exhibits a high ionic conductivity of $3.51 \times 10^{-4}$ S cm$^{-1}$ at 20 °C, which is higher than that of ANF ($2.08 \times 10^{-5}$ S cm$^{-1}$) and T-ANF-MOF ($1.49 \times 10^{-4}$ S cm$^{-1}$) (Figure 3b). The corresponding Arrhenius plots of the R-ANF-MOF, T-ANF-MOF, and ANF based on ionic conductivity are illustrated in Figure 3c. According to the Arrhenius equation and the corresponding linear fitting curve,

the Li$^+$ transport activation energy is further calculated. It can be observed from Figure S25 that R-ANF-MOF exhibits a significantly lower Li$^+$ transport activation energy of 0.11 eV compared with T-ANF-MOF (0.15 eV) and ANF (0.22 eV), thereby facilitating enhanced rapid transportation of Li$^+$. As another pivotal aspect of QSSE, the polarization curves and initial and steady-state impedance spectra in Li||Li symmetric cells were evaluated (Figure S26 and Table S4). As shown in Figure 3d, the calculated Li$^+$ transference number for R-ANF-MOF is 0.85, which is superior to ANF (0.21) and T-ANF-MOF (0.76), this result manifests that the R-ANF-MOF has the outstanding single-ion transport capacity. Benefitting from the interfacial coupling generated by the atomic structure rearrangement between the amorphous structure of R-ANF and ANF, not only is the distance for Li$^+$ migration shortened, but also the kinetics of Li$^+$ transport are promoted. This leads to a significant reduction in local ion concentration and facilitates homogeneous deposition of lithium. In contrast, the crystalline-amorphous interface structure mismatch of T-ANF-MOF results in the hindrance of Li$^+$ transport and the nonuniform distribution of Li$^+$ concentration (Figure 3e).

To further identify the influence of different structures of MOF and ANF, the Li plating/stripping behavior was additionally evaluated using Li|QSSE|Li symmetric cells under galvanostatic conditions, with a constant current density corresponding to an areal capacity of 0.1 mAh cm$^{-2}$. As represented in Figure 3f, the Li|R-ANF-MOF|Li exhibits stable Li plating/stripping for more than 1500 h with a low voltage hysteresis. By comparison, the Li|T-ANF-MOF|Li and Li|ANF|Li display a short occurred after cycling for a short period of time (<500 h). The symmetrical battery with R-ANF-MOF demonstrated much lower overpotential (58 mV) than ANF (187 mV) and T-ANF-MOF (94 mV) after stable Li plating/stripping. In addition, the surface morphology of lithium anodes following Li plating/stripping was further characterized by SEM (Figure S27). The surface of the lithium anode in the Li|R-ANF-MOF|Li symmetrical cell is relatively smooth and no obvious Li dendrites are surveyed, by contrast, the surface of the lithium anode symmetrical cell has more disorderly raised Li dendrites. The continuous amorphous structure of R-ANF and its excellent amorphous-amorphous interface contact with ANF contribute to the faster Li$^+$ transport paths and more effective ion transport, in the Li|T-ANF-MOF|Li symmetrical cell has slightly aggregated Li dendrites, and the surface of lithium anode in the Li|ANF|Li which facilitates the smooth deposition of Li$^+$ and thus restrains the generation of Li dendrites. To further investigate the migration of Li$^+$ on different structure MOFs and between ANF and MOF interfaces, the diffusion barriers for Li$^+$ on the R-MOF, T-MOF, ANF/R-MOF interface, and ANF/T-MOF interface were implemented. As illustrated in Figure 3g–h, the calculated results reveal that R-MOF (0.5939 eV) has a lower migration barrier compared with T-MOF (0.749 eV). In addition, Li$^+$ can easily migrate across the ANF/R-MOF interface with a barrier energy of only 1.057 eV, which is lower compared with ANF/T-MOF (1.144 eV). The calculated outcomes exhibit a high degree of matching with the previous experimental findings and confirm that the R-ANF-MOF as QSSE effectively accelerates rapid diffusion
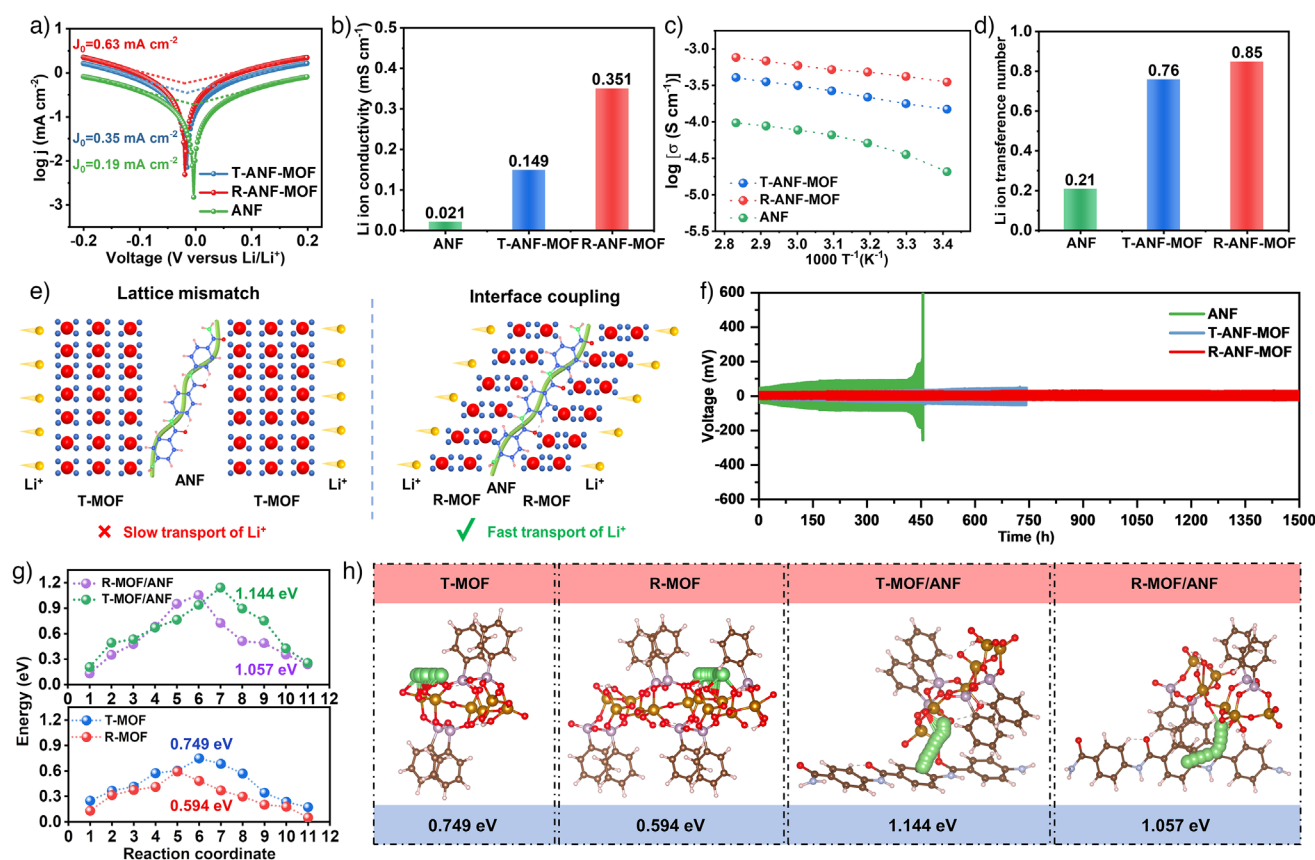
**Figure 3.** a) Tafel plots for Li plating/stripping of the Li‖Li cells with ANF, R-ANF-MOF, and T-ANF-MOF. b) Li$^+$ conductivity, c) Arrhenius plots of the ionic conductivities, and d) Li$^+$ transference number of ANF, T-ANF-MOF, and R-ANF-MOF. e) The schematic of the transport mechanism of Li$^+$ in T-MOF-ANF and R-MOF-ANF. f) Galvanostatic cycling performance of the Li‖Li symmetrical cells with ANF, T-ANF-MOF, and R-ANF-MOF at 0.1 mA cm$^{-2}$ for 0.1 mAh cm$^{-2}$. g) Energy profiles and h) pathway of Li$^+$ migration on T-MOF, R-MOF, T-MOF-ANF, and R-MOF-ANF substrates.

kinetics in Li deposition and restrains the generation of the Li dendrites.

To evaluate the practical application potential of different QSSE membranes, the full cells are first assembled with a lithium anode and LiFePO$_4$ (LFP) cathode and QSSE membrane. As shown in Figure S28, the LFP‖R-ANF-MOF‖Li quasi-solid-state battery performs with a high initial specific capacity of 176 mAh g$^{-1}$ and a stable cycle performance of more than 800 cycles at 1 C, the capacity retention rate is 86.2%. In particular, the LFP‖R-ANF-MOF‖Li quasi-solid-state battery still shows a high initial specific capacity of 139.4 mAh g$^{-1}$ and a long cycle of more than 8000 cycles, and the capacity retention rate is 64% at the high rate of 5 C (Figure S29). In addition, the full cells are also assembled with high-voltage LiNi$_{0.8}$Co$_{0.1}$Mn$_{0.1}$O$_2$ (NCM811) cathode and R-ANF-MOF QSSE to further evaluate the electrochemical performance. The NCM811‖R-ANF-MOF‖Li quasi-solid-state battery performs with a high initial specific capacity of 154.7 mAh g$^{-1}$ at 1 C and achieves a capacity retention rate of 85.1% after 300 cycles (Figure S30). Figure S31 demonstrates the satisfactory rate performance of NCM811‖R-ANF-MOF‖Li cells.

To further investigate the effect of amorphous structure and amorphous–amorphous architecture on the electrochem-

ical performance of Li–I$_2$ cells, the full Li–I$_2$ cells were assembled with I$_2$/C cathode, QSSE membranes, and Li anode. As shown in Figure 4a, the CV curve of R-ANF-MOF displays two anodic and two cathodic peaks located at 2.91/2.86 and 3.32/3.29 V, which is ascribed to the multistep reversible oxidation and reduction reaction of I$_2$/I$^-$. The battery with R-ANF-MOF exhibits a lower potential polarization than T-ANF-MOF, indicating that the structure of R-ANF-MOF improved the oxidation overpotential. Furthermore, the CV curves of the Li–I$_2$ cells with R-ANF-MOF and T-ANF-MOF were obtained at 0.1–0.5 mV s$^{-1}$ scan rate (Figure S32a,c). The Li$^+$ diffusion coefficient was investigated by analyzing the corresponding linear relation between peak current ($I_p$) and the square root of the scan rate. As depicted in Figure S32b,d, R-ANF-MOF exhibits a higher Li$^+$ diffusion coefficient compared to T-ANF-MOF at peaks 1 and 2, demonstrating faster migration behavior of Li$^+$. The electrochemical impedance spectroscopy (EIS) was further explored to investigate the interfacial behavior and reversibility of Li–I$_2$ cells (Figure S33). The cell with R-ANF-MOF displays a lower charge transfer resistance ($R_{ct} = 62\ \Omega$) in comparison to T-ANF-MOF (133 $\Omega$), indicating its superior interfacial charge transfer capability.

Furthermore, the rate performance of Li–I$_2$ batteries with different R-ANF-MOF and T-ANF-MOF QSSE membranes
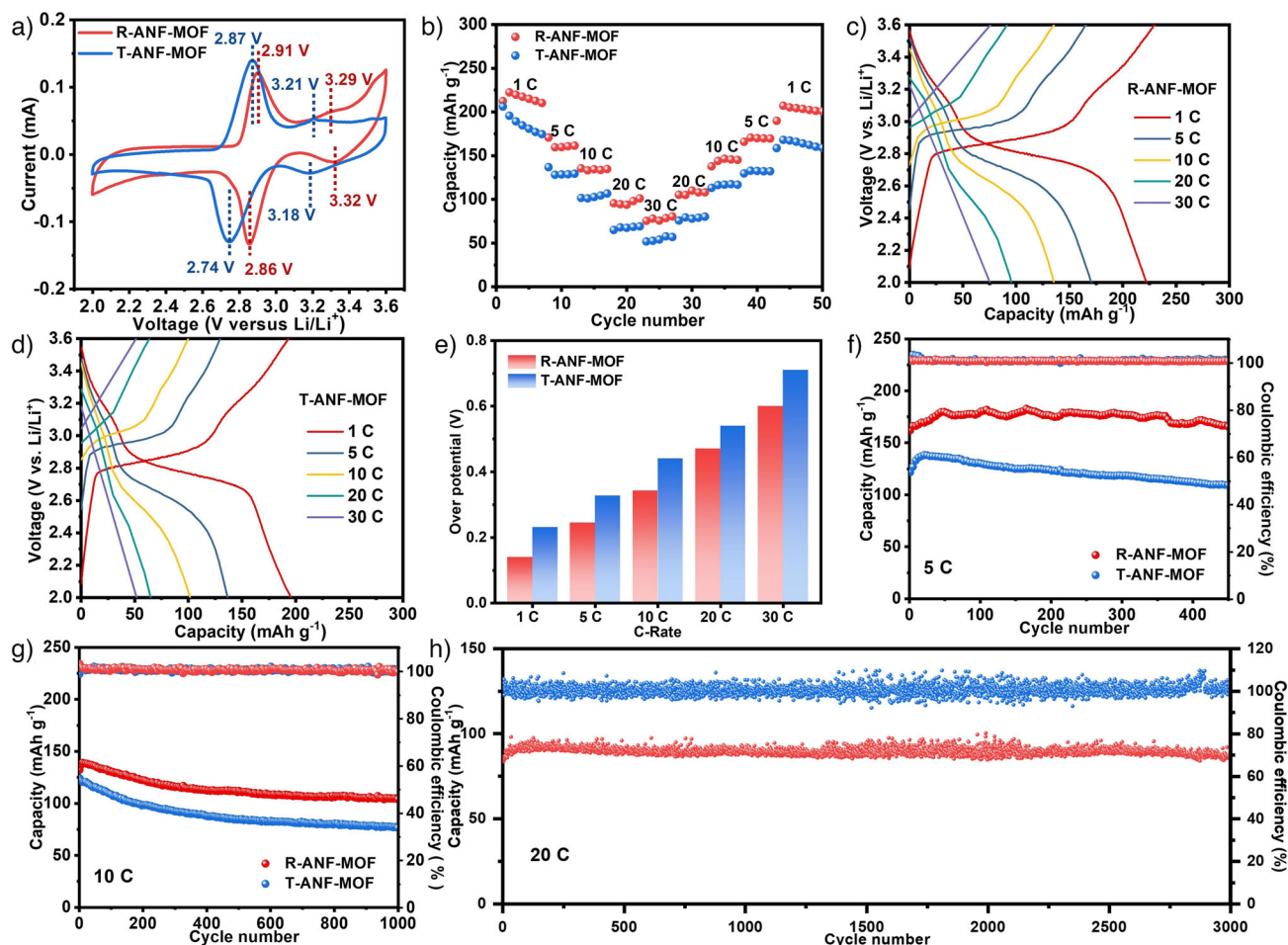
*Angew. Chem. Int. Ed.* **2025**, *64*, e202507184 (6 of 10)

© 2025 Wiley-VCH GmbH

**Figure 4.** Electrochemical performance of the Li–I$_2$ cells with various QSSEs. a) CV curves. b) Rate performance. c) and d) Galvanostatic charge–discharge profiles of (c) R-ANF-MOF and (d) T-ANF-MOF at different rates. e) The overpotential at different rates. f) and g) Cycling performance at (f) 5 C and (g) 10 C. h) Long-term performance at a current density of 20 C.

was measured at the current densities ranging from 1 to 30 C. As shown in Figure 4b, the R-ANF-MOF reveals the specific discharge capacities of 212.5, 170.1, 135.5, 95.6, and 75.5 mAh g$^{-1}$ at 1, 5, 10, 20, and 30 C, respectively. Remarkably, the reversible capacity of 200.8 mAh g$^{-1}$ can be achieved when the current density is reduced to 1 C again, signifying the exceptional rate performance. The voltage curves for charge and discharge at different current rates are depicted in Figure 4c,d, and the polarization voltage of R-ANF-MOF and T-ANF-MOF exhibits a significant increase with increasing current density. Notably, the R-ANF-MOF demonstrates lower polarization voltage values compared to T-ANF-MOF at various current rates (Figure 4e). The electrochemical performance of Li–I$_2$ batteries with various QSSE membranes at 5 C was further evaluated (Figure 4f). The Li–I$_2$ cell equipped with the R-ANF-MOF exhibits a higher initial capacity of 170.7 mAh g$^{-1}$ and a superior capacity retention of 166.9 mAh g$^{-1}$ after 450 cycles, which is significantly advantageous compared to the T-ANF-MOF QSSE membrane. In contrast, ANF as the electrolyte is unable to maintain long-term stable cycle performance even at 1 C due to its poor ionic conductivity and dense structure

(Figure S34). Notably, the Li–I$_2$ cell assembled with R-ANF-MOF initially shows a discharge capacity of 131.9 mAh g$^{-1}$ and maintains an invertible capacity of 105.4 mAh g$^{-1}$ after 1000 cycles at 10 C, accompanied by a low attenuation rate of only 0.0002% per cycle, whereas the T-ANF-MOF QSSE membrane only delivers an initial discharge capacity of 122.6 mAh g$^{-1}$ and maintains an invertible capacity of merely 76.4 mAh g$^{-1}$ after 1000 cycles (Figure 4g). The long-term cycling stability of Li–I$_2$ batteries was further investigated under a higher current density of 20 C (Figure 4h). The Li–I$_2$ cells with R-ANF-MOF demonstrate excellent cycling stability with a reversible capacity of 88.8 mAh g$^{-1}$ over 3000 cycles, indicating sufficient suppression ability of the polyiodide shuttle. This work exhibits remarkable advantages when compared with other strategies (Table S5), demonstrating the state-of-the-art performance of R-ANF-MOF in Li–I$_2$ batteries. To monitor the dendrite growth on the Li anodes of the Li–I$_2$ battery after the cycle, the Li–I$_2$ cell was disassembled after the cycling test at 5 C. As shown in Figure S35, it can be clearly observed through optical photos and SEM that the surface of the Li foil surface of Li–I$_2$ cell with R-ANF-MOF was relatively smooth and dense, and no
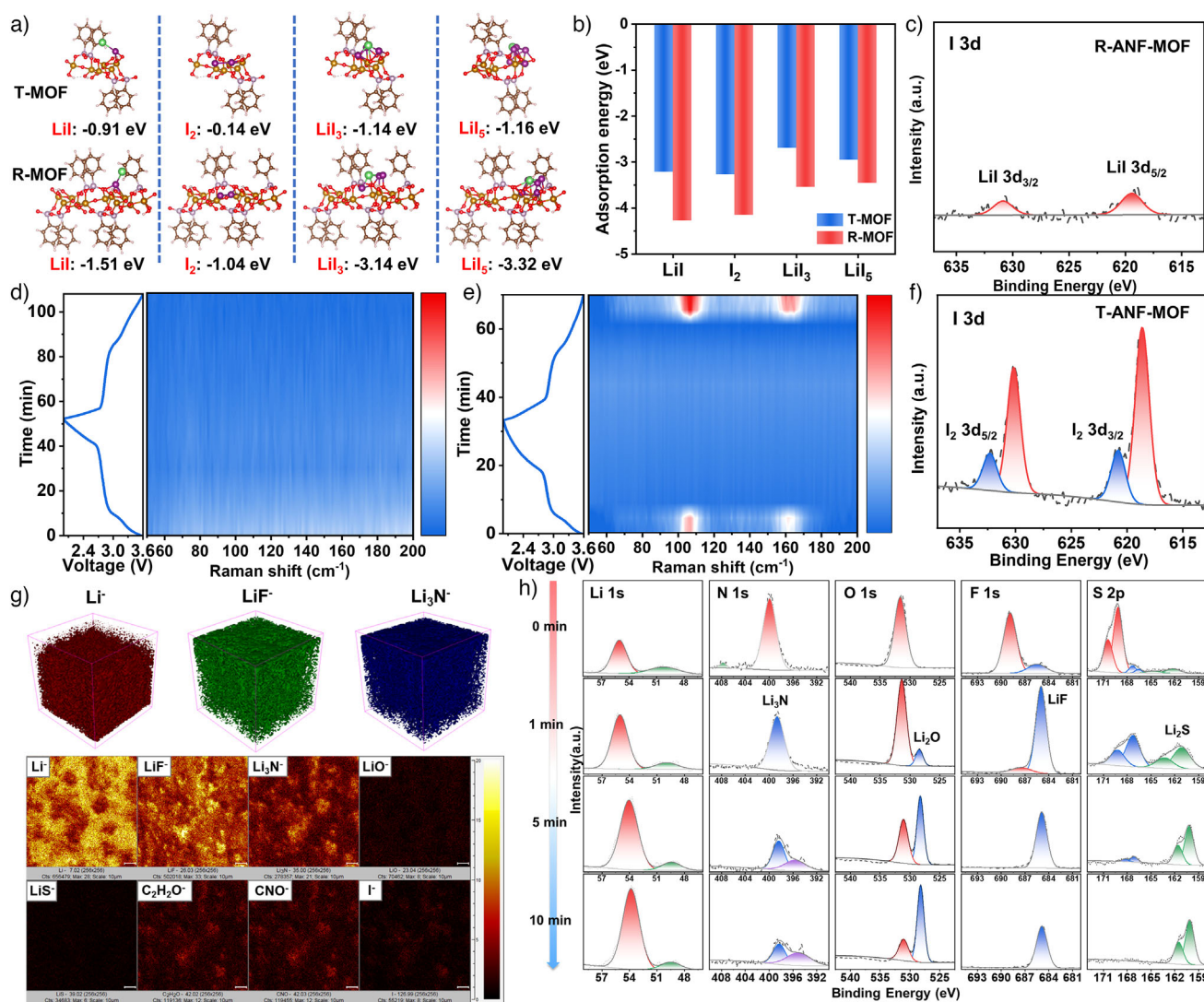
**Figure 5.** a) The optimized adsorption configurations and b) the calculated adsorption energies of LiI, $I_2$, LiI$_3$, and LiI$_5$ interacted with T-MOF and R-MOF substrates. c)–f) High-resolution XPS spectra of I 3d for the cycled Li anodes paired with (c) R-ANF-MOF and (f) T-ANF-MOF. d) and e) The in situ Raman spectroscopy obtained during the charge/discharge processes with (d) R-ANF-MOF and (e) T-ANF-MOF. g) TOF-SIMS 3D and 2D spectra of different secondary ions for the Li anode surface of the R-ANF-MOF. h) A depth profiling of the elements on the Li anode surface of the R-ANF-MOF by the XPS sputter etching technique.

Li dendrite was generated, while the Li anode surface of Li–$I_2$ cell with T-ANF-MOF was cluttered with undesired corrosion and pulverization. A single-layer pouch cell was fabricated to further explore the practical potential of R-ANF-MOF. The pouch cell can readily support the continuous working of the green light-emitting diode (LED) indicator (Figure S36). The density functional theory (DFT) calculations were implemented to explore the interaction energy between different structures of MOFs and iodine species. The iodine species include different I-related molecules such as LiI, $I_2$, LiI$_3$, and LiI$_5$ are investigated. The optimized adsorption configurations and the corresponding adsorption energies of LiI, $I_2$, LiI$_3$, and LiI$_5$ on MOFs are shown in Figure 5a,b, It was noted that R-MOF delivers binding energies of −1.51, −1.04, −3.14, and −3.32 eV with LiI, $I_2$, LiI$_3$, and LiI$_5$, respectively, surpassing those observed

on T-MOF (−0.91, −0.14, −1.14, and −1.16 eV with LiI, $I_2$, LiI$_3$, and LiI$_5$, respectively), further verifying the strong chemical interactions between R-MOF and iodine species. Furthermore, the trapping ability toward the intermediate product of the iodine cathode was further performed by a visualized adsorption experiment as depicted in Figure S37. It can be clearly observed that there is a significant amount of polyiodide diffusion when the ANF membrane is used as a blocking layer after 1 h. For T-ANF-MOF, the permeation of polyiodide through the T-ANF-MOF membrane is evidently slowed down, but it also exhibits obvious penetration after 36 h. Satisfactorily, the color of the electrolyte of R-ANF-MOF remains colorless even after adsorption at room temperature for 36 h, thereby indicating the exceptional anchoring capability of R-ANF-MOF toward soluble iodide species.

*Angew. Chem. Int. Ed.* **2025**, *64*, e202507184 (8 of 10)

© 2025 Wiley-VCH GmbH

The X-ray photoelectron spectroscopy on Li anode surface of the cell with R-ANF-MOF and T-ANF-MOF after 50 cycles was also acquired to identify the shuttle of polyiodides. As shown in Figure 5c,f, the I 3d spectrogram data reveals small characteristic peaks of Li anode surface with R-ANF-MOF at 630.8 and 619.4 eV, corresponding to LiI. As a contrast, Li anode surface with T-ANF-MOF displays intense characteristic peaks assigned to the LiI and $I_2$ appear at 632.2 and 620.8 eV. The inhibition of QSSE membrane on the shuttle effect of polyiodides during cycling was further performed by in situ Raman spectroscopy (Figure S38). Figure 5d,e present the time-resolved Raman contour maps of the batteries equipped with R-ANF-MOF and T-ANF-MOF at different discharge states. As shown in Figure 5e, the signal peaks of the cell with T-ANF-MOF at around 106.4 and 161.7 cm$^{-1}$ were observed during the continuous discharge process, which belonged to the characteristics $I_3^-$ and $I_5^-$, respectively, indicating the severe polyiodides shuttle behavior. By comparison, the cell with R-ANF-MOF exhibits negligible signals of $I_3^-$ and $I_5^-$ in the continuous discharge process (Figure 5d), demonstrating the ability of R-ANF-MOF to effectively suppress the shuttle effect of polyiodides. The aforementioned findings convincingly verify that the utilization of R-ANF-MOF QSSE effectively suppresses the shuttle effect of polyiodides, thereby enhancing the performance of Li–$I_2$ batteries.

The stable solid electrolyte interphase (SEI) layer is crucial to suppressing the formation of Li dendrites and enhancing the performance of Li–$I_2$ batteries. The time-of-flight secondary ion mass spectrometry (ToF-SIMS) characterization on the surface of cycled Li anode was conducted to investigate the main components and their distribution within SEI formed during cycling. The 2D spectra and 3D reconstruction results of R-ANF-MOF and T-ANF-MOF after 50 cycles at 1 C are shown in Figures 5g and S39. The Li anode on the top surface with R-ANF-MOF exhibits the significant signal intensity of inorganic SEI layers (such as LiF$^-$ and Li$_3$N$^-$) and organic components (such as C$_2$H$_2$O$^-$), which were attributed to the decomposition of electrolyte salts and the reduction of ether-based electrolyte.[35] As the sputtering time increases, it becomes evident that R-ANF-MOF exhibits a denser and thicker inorganic SEI layer compared to T-ANF-MOF. Furthermore, the 2D spectra for I$^-$ ionic fragments reveal no presence of iodine species shuttling from the anode of the cell equipped with R-ANF-MOF, the ToF-SIMS analysis is consistent with the experimental results mentioned above. Meanwhile, the composition of the SEI layer on the Li anode was further confirmed by XPS etching. As shown in Figure 5h, in the Li 1s spectra, the peaks are assigned to inorganic components such as LiF, Li$_2$O, Li$_2$S, Li$_3$N, and lithium metal. In the spectra of F 1s, O 1s, N 1s, and S 2p, the corresponding characteristic peaks of inorganic components such as LiF, Li$_2$O, Li$_3$N, and Li$_2$S were significantly enhanced with increasing etching time when compared to T-ANF-MOF (Figure S40), indicating that R-MOF accelerates the decomposition of LiTFSI.[36] These results further demonstrate that stable inorganic components of SEI films containing LiF, Li$_2$O, Li$_3$N, and Li$_2$S on the surface of Li anode significantly inhibit the growth of Li dendrites and enhance the stability and safety of the battery.

## Conclusion

In summary, we have developed an atomic structure rearrangement of MOFs to achieve novel combinations between MOFs and polymers. On one hand, the amorphous engineering facilitates compact interface contact, thereby enhancing the migration kinetics and reducing the migration distance of Li$^+$. On the other hand, the highly exposed active site improves polyiodide adsorption, resulting in a significant enhancement in the performance of the capacity and cycle stability of Li–$I_2$ batteries. The amorphous structure of R-MOF was verified by selected area electron diffraction (SAED), XANES, and X-ray PDF spectra, and the working mechanism of R-ANF-MOF electrolyte was revealed by employing in situ Raman, ToF-SIMS, XPS etching, and DFT calculations. The cells with R-ANF-MOF continuous interface electrolyte exhibited a high specific capacity of 170.7 mAh g$^{-1}$ at 5 C and satisfactory rate performance with a capacity of 75.5 mAh g$^{-1}$ at 30 C. Remarkably, the cells received the excellent cycle stability by enduring up to 3000 cycles at high current density of 20 C and maintained an exceptionally low capacity decay rate of merely 0.0002% per cycle. This work presents compelling evidence regarding the potential application of quasi-solid-state Li–$I_2$ batteries for energy storage requiring high safety and high capacity.

## Conflict of Interests

The authors declare no conflict of interest.

## Data Availability Statement

The data that support the findings of this study are available from the corresponding author upon reasonable request.

[1] J. Z. Ma, M. M. Liu, Y. L. He, J. T. Zhang, *Angew. Chem. Int. Ed.* **2021**, *60*, 12636–12647.

[2] C. Sun, X. L. Shi, Y. B. Zhang, J. J. Liang, J. Qu, C. Lai, *ACS Nano* **2020**, *14*, 1176–1184.

[3] P. Li, X. Li, Y. Guo, C. Li, Y. Hou, H. Cui, R. Zhang, Z. Huang, Y. Zhao, Q. Li, B. Dong, C. Zhi, *Adv. Energy Mater.* **2022**, *12*, 2103648.

[4] S. Tan, X. Feng, Y. Wang, Y. Guo, S. Xin, *ACS Appl. Mater. Interfaces* **2024**, *16*, 67002–67009.

[5] X. Li, Y. Wang, J. Lu, S. Li, P. Li, Z. Huang, G. Liang, H. He, C. Zhi, *Angew. Chem. Int. Ed.* **2023**, *62*, e202310168.

[6] F. Zhu, Z. Li, Z. Wang, Y. Fu, W. Guo, *J. Am. Chem. Soc.* **2024**, *146*, 11193–11201.

[7] X. Li, Y. Zhu, S. Tan, S. Xin, *Batteries Supercaps* **2024**, *7*, e202300572.

[8] Y. Jiang, P. Huang, M. Tong, B. Qi, T. Sun, Z. Xian, W. Yan, C. Lai, *Carbon Energy* **2024**, *6*, e478.

[9] X. Tang, D. Zhou, P. Li, X. Guo, C. Wang, F. Kang, B. Li, G. Wang, *ACS Cent. Sci.* **2019**, *5*, 365–373.

[10] Z. Cheng, H. Pan, F. Li, C. Duan, H. Liu, H. Zhong, C. Sheng, G. Hou, P. He, H. Zhou, *Nat. Commun.* **2022**, *13*, 125.

[11] X. Li, Y. Zhao, Y. Zhu, W. Wang, Y. Zhang, F. Wang, Y. Guo, S. Xin, C. Bai, *Proc. Natl. Acad. Sci. USA* **2024**, *121*, e2316564121.

[12] X. Hu, Z. Zhang, X. Zhang, Y. Wang, X. Yang, X. Wang, M. Fayena-Greenstein, H. A. Yehezkel, S. Langford, D. Zhou, B. Li, G. Wang, D. Aurbach, *Nat. Rev. Mater.* **2024**, *9*, 305–320.

[13] Y. M. Jin, R. F. Lin, Y. M. Li, X. B. Zhang, S. P. Tan, Y. Shuai, Y. P. Xiong, *Angew. Chem. Int. Ed.* **2024**, *63*, e202403661.

[14] X. Rui, R. Hua, D. Ren, F. Qiu, Y. Wu, Y. Qiu, Y. Mao, Y. Guo, G. Zhu, X. Liu, Y. Gao, C. Zhao, X. Feng, L. Lu, M. Ouyang, *Adv. Mater.* **2024**, *36*, 2402401.

[15] T. Hou, W. Xu, X. Pei, L. Jiang, O. M. Yaghi, K. A. Persson, *J. Am. Chem. Soc.* **2022**, *144*, 13446–13450.

[16] P. Dong, X. Zhang, W. Hiscox, J. Liu, J. Zamora, X. Li, M. Su, Q. Zhang, X. Guo, J. McCloy, M. K. Song, *Adv. Mater.* **2023**, *35*, 2211841.

[17] Z. Chang, H. J. Yang, X. Y. Zhu, P. He, H. S. Zhou, *Nat. Commun.* **2022**, *13*, 1510.

[18] Y. Zheng, N. Yang, R. Gao, Z. Li, H. Dou, G. Li, L. Qian, Y. Deng, J. Liang, L. Yang, Y. Liu, Q. Ma, D. Luo, N. Zhu, K. Li, X. Wang, Z. Chen, *Adv. Mater.* **2022**, *34*, 2203417.

[19] W. Huang, S. Wang, X. Zhang, Y. Kang, H. Zhang, N. Deng, Y. Liang, H. Pang, *Adv. Mater.* **2023**, *35*, 2310147.

[20] S. Duan, L. Qian, Y. Zheng, Y. Zhu, X. Liu, L. Dong, W. Yan, J. Zhang, *Adv. Mater.* **2024**, *36*, 2314120.

[21] Y. Liu, S. Wang, W. Chen, W. Kong, S. Wang, H. Liu, L. Ding, L. X. Ding, H. Wang, *Adv. Mater.* **2024**, *36*, 2401837.

[22] L. Bi, J. Xiao, Y. Song, T. Sun, M. Luo, Y. Wang, P. Dong, Y. Zhang, Y. Yao, J. Liao, S. Wang, S. Chou, *Carbon Energy 6*, e544.

[23] R. A. Tong, Y. Huang, C. Feng, Y. Dong, C. A. Wang, *Adv. Funct. Mater.* **2024**, *34*, 2315777.

[24] H. Peng, T. Long, J. Peng, H. Chen, L. Ji, H. Sun, L. Huang, S. G. Sun, *Adv. Energy Mater.* **2024**, *14*, 2400428.

[25] J. Zhang, J. Chou, X. X. Luo, Y. M. Yang, M. Y. Yan, D. Jia, C. H. Zhang, Y. H. Wang, W. P. Wang, S. J. Tan, J. C. Guo, Y. Zhao, F. Wang, S. Xin, L. J. Wan, Y. G. Guo, *Angew. Chem. Int. Ed.* **2024**, *63*, e202316087.

[26] Y. Xiang, L. Zhou, P. Tan, S. Dai, Y. Wang, S. Bao, Y. Lu, Y. Jiang, M. Xu, X. Zhang, *ACS Nano* **2023**, *17*, 19275–19287.

[27] E. V. Shaw, A. M. Chester, G. P. Robertson, C. Castillo-Blas, T. D. Bennett, *Chem. Sci.* **2024**, *15*, 10689–10712.

[28] S.-H. Lo, L. Feng, K. Tan, Z. Huang, S. Yuan, K.-Y. Wang, B.-H. Li, W.-L. Liu, G. S. Day, S. Tao, C.-C. Yang, T.-T. Luo, C.-H. Lin, S.-L. Wang, S. J. L. Billinge, K.-L. Lu, Y. J. Chabal, X. Zou, H.-C. Zhou, *Nat. Chem.* **2020**, *12*, 90–97.

[29] F. Li, X. B. Cheng, G. X. Lu, Y. C. Yin, Y. C. Wu, R. J. Pan, J. D. Luo, F. Y. Huang, L. Z. Feng, L. L. Lu, T. Ma, L. R. Zheng, S. H. Jiao, R. G. Cao, Z. P. Liu, H. M. Zhou, X. Y. Tao, C. Shang, H. B. Yao, *J. Am. Chem. Soc.* **2023**, *145*, 27774–27787.

[30] H. Zhang, S. Liu, A. Zheng, P. Wang, Z. Zheng, Z. Wang, H. Cheng, Y. Dai, B. Huang, Y. Liu, *Angew. Chem. Int. Ed.* **2024**, *63*, e202400965.

[31] S. Zheng, H. Zhang, J. Fan, Q. Xu, Y. Min, *Small* **2021**, *17*, 2102347.

[32] B. Yang, L. Wang, M. Zhang, J. Luo, X. Ding, *ACS Nano* **2019**, *13*, 7886–7897.

[33] W. Xing, S. Yin, W. Tu, G. Liu, S. Wu, H. Wang, M. Kraft, G. Wu, R. Xu, *Angew. Chem. Int. Ed.* **2020**, *59*, 1171–1175.

[34] S. Chen, A. Tennakoon, K.-E. You, A. L. Paterson, R. Yappert, S. Alayoglu, L. Fang, X. Wu, T. Y. Zhao, M. P. Lapak, M. Saravanan, R. A. Hackler, Y.-Y. Wang, L. Qi, M. Delferro, T. Li, B. Lee, B. Peters, K. R. Poeppelmeier, S. C. Ammal, C. R. Bowers, F. A. Perras, A. Heyden, A. D. Sadow, W. Huang, *Nat. Catal.* **2023**, *6*, 161–173.

[35] X. Zhang, Q. Su, G. Du, B. Xu, S. Wang, Z. Chen, L. Wang, W. Huang, H. Pang, *Angew. Chem. Int. Ed.* **2023**, *62*, e202304947.

[36] Y. Li, M. Liu, K. Wang, C. Li, Y. Lu, A. Choudhary, T. Ottley, D. Bedrov, L. Xing, W. Li, *Adv. Energy Mater.* **2023**, *13*, 2300918.